JAMES | Journal of Advances in Modeling Earth Systems®

RESEARCH ARTICLE
10.1029/2024MS004615

Insights on Tropical High-Cloud Radiative Effect From a New Conceptual Model

Jakob Deutloff[1,2], **Stefan A. Buehler**[1], **Manfreth Brath**[1], **and Ann Kristin Naumann**[1,3]

[1]Center for Earth System Research and Sustainability (CEN), Meteorological Institute, Universität Hamburg, Hamburg, Germany, [2]International Max Planck Research School on Earth System Modelling (IMPRS-ESM), Hamburg, Germany, [3]Max Planck Institute for Meteorology, Hamburg, Germany

Key Points:

- The complexity of tropical high-cloud radiative effect is reduced by conceptualizing it as a function of the ice water path
- High clouds within our model simulation are characterized by a weakly positive high-cloud radiative effect
- Low clouds render the high-cloud radiative effect positive

Correspondence to:
J. Deutloff,
jakob.deutloff@uni-hamburg.de

Citation:
Deutloff, J., Buehler, S. A., Brath, M., & Naumann, A. K. (2025). Insights on tropical high-cloud radiative effect from a new conceptual model. *Journal of Advances in Modeling Earth Systems*, *17*, e2024MS004615. https://doi.org/10.1029/2024MS004615

Received 1 AUG 2024
Accepted 8 FEB 2025

Author Contributions:
Conceptualization: Jakob Deutloff, Stefan A. Buehler, Ann Kristin Naumann
Data curation: Jakob Deutloff, Manfreth Brath
Funding acquisition: Stefan A. Buehler, Ann Kristin Naumann
Investigation: Jakob Deutloff
Methodology: Jakob Deutloff, Stefan A. Buehler, Manfreth Brath, Ann Kristin Naumann
Project administration: Stefan A. Buehler, Ann Kristin Naumann
Software: Jakob Deutloff, Manfreth Brath
Supervision: Stefan A. Buehler, Ann Kristin Naumann
Visualization: Jakob Deutloff
Writing – original draft: Jakob Deutloff
Writing – review & editing: Jakob Deutloff, Stefan A. Buehler, Ann Kristin Naumann

Abstract The new capabilities of global storm-resolving models to resolve individual clouds allow for a more physical perspective on the tropical high-cloud radiative effect and how it might change with warming. In this study, we develop a conceptual model of the high-cloud radiative effect as a function of cloud thickness measured by ice water path. We use atmospheric profiles from a global ICON simulation with 5 km horizontal grid spacing to calculate the radiation offline with the ARTS line-by-line radiative transfer model. The conceptual model of the high-cloud radiative effect reveals that it is sufficient to approximate high clouds as a single layer characterized by an albedo, emissivity and temperature, which vary with ice water path. The increase of the short-wave high-cloud radiative effect with ice water path is solely explained by the high-cloud albedo. The increase of the long-wave high-cloud radiative effect with ice water path is governed by an increase of emissivity for ice water path below 10^{-1} kg m^{-2}, and by a decrease of high-cloud temperature with increasing ice water path above this threshold. The mean high-cloud radiative effect from the ARTS simulations for the chosen day of this ICON model run is 1.25 W m^{-2}, which is closely matched by our conceptual model with 1.26 W m^{-}2. Because the high-cloud radiative effect depends on the assumed radiative alternative, assumptions on low clouds make a substantial difference. The conceptual model predicts that doubling the fraction of low clouds roughly doubles the positive high-cloud radiative effect.

Plain Language Summary High clouds are widespread within the tropics and can either amplify or dampen global warming if they change in a way that affects their ability to reflect solar or absorb terrestrial thermal radiation. To better understand how high clouds within the tropics might influence global warming, we use high-resolution climate models that are able to resolve individual clouds. Those models allow us to interpret the effect of high clouds on solar and thermal radiation as a function of the cloud thickness. To better understand this dependence, we develop a conceptual model of high clouds that breaks the physical mechanisms down to their main parts. The conceptual model shows that high clouds can be well approximated as a single layer whose reflectivity, temperature and transparency to thermal radiation depend on the cloud thickness. We find that high clouds are slightly warming the Earth in the current climate, which is well reproduced by the conceptual model. The conceptual model reveals that if more low clouds exist below the high clouds, the warming effect of high clouds is increased.

1. Introduction

Cloud feedbacks remain to contribute most to the uncertainty in climate sensitivity among all feedback processes (Arias et al., 2021). Splitting up the cloud feedback into its subcomponents reveals that the major part of the net uncertainty associated with it stems from tropical high clouds (Sherwood et al., 2020). They can produce a climate feedback if their radiative effect changes in response to surface warming. To reduce the uncertainty within the tropical high-cloud feedback, it is therefore necessary to understand what controls the tropical high-cloud radiative effect (C) and how it might change with warming, which is the aim of this study.

Most analysis of tropical high-cloud feedbacks is based on global circulation models (GCMs) with horizontal resolutions $\mathcal{O}$(100 km) (Bony et al., 2016; Mauritsen & Stevens, 2015). Since GCMs are not able to resolve individual clouds, they predict the fraction of a grid cell covered with clouds. This has led to the notion of approximating high clouds to be uniform with an average albedo, emissivity, altitude and extent (McKim et al., 2024). The common analysis of the high-cloud feedback is based on this approximation. Therefore, the high-cloud feedback is often decomposed into an altitude, amount and optical thickness contribution

(McKim et al., 2024; Sherwood et al., 2020; Zelinka et al., 2022). The high-cloud altitude feedback is expected to be positive, since tropical high clouds will rise and warm less than the surface in case of global warming and thereby mask the Planck feedback. This hypothesis is referred to as the proportionally higher anvil temperature (PHAT) mechanism (Zelinka & Hartmann, 2010). Similar thermodynamic arguments suggest that the tropical high-cloud amount will decrease, resulting in a negative feedback, which is referred to as the stability iris (Bony et al., 2016). Changes in high-cloud optical thickness have the potential for a strong feedback, but remain unconstrained (McKim et al., 2024).

This decomposition of the high-cloud feedback rests on the assumption of an average C, which was found to be near-neutral (Hartmann, 2016) with single estimates ranging from to weakly negative to weakly positive (-1.5 W m^{-2} found by McKim et al. (2024), 2 W m^{-2} found by L'Ecuyer et al. (2019)). However, satellite observations resolving the clouds at a much higher resolution than GCMs ($\mathcal{O}$(5 km)) have shown that approximating high clouds to be uniform with an average C is highly inaccurate (Berry & Mace, 2014). The radiative properties of high clouds vary with the cloud thickness, which can be measured by the ice water path (I). Since I of high clouds spans several orders of magnitude, associated with very different C, neglecting this dependence risks missing important feedbacks that do not map onto the oversimplified coordinates of mean altitude, mean amount and mean optical thickness.

The development of global storm resolving models (GSRMs), with horizontal resolutions $\mathcal{O}$(5 km), makes it possible to resolve C as a function of I in global simulations. The usefulness of this perspective on model simulations has recently been shown by Sokol et al. (2024), who applied it to radiative-convective equilibrium simulations. With this study, we aim to harness the new capabilities of GSRMs to further develop the ice water path perspective on C. We show that this perspective is deeply rooted within the physics underlying C by constructing a conceptual model that explains the dependence of C on I. This conceptual model reduces the complexity of C significantly, and hence provides a framework to evaluate the high-cloud feedback within warming GSRM simulations, which can replace the overly simplistic decomposition that was made for GCMs. Resolving C as a function of I allows to understand how the contribution of high clouds with a specific I to the mean C is governed by their $C(I)$ as well as their frequency of occurrence. We believe that this ice water perspective on the high-cloud radiative effect can provide new insights about the high-cloud feedback beyond the established decomposition.

After presenting our model setup in Section 2, we explain how C can be interpreted as a function of I in Section 3. We use this perspective to construct the conceptual model of $C(I)$ (Section 4), which helps us to understand its key ingredients (Section 5). The role of low clouds for C is investigated in Section 6. We give an outlook on how the conceptual model can be useful for analyzing high-cloud feedbacks in Section 7, before we conclude with Section 8. We explain our methods in depth in Section 9.

2. Model Setup

Our conceptual model rests upon the development of global storm-resolving models (GSRMs) which explicitly resolve deep convection in the tropics. In particular, we use instantaneous atmospheric profiles from global simulations with the ICOsahedral Nonhydrostatic weather and climate model (ICON) (Hohenegger et al., 2023) with 5 km horizontal grid spacing. Microphysical processes within ICON are parameterized with a one-moment scheme, which distinguishes five hydrometeors: cloud water, rain, cloud ice, snow, and graupel (Baldauf et al., 2011). ICON is forced with pre-industrial sea surface temperature from CMIP6 models and run for 6 months (Kluft, 2023). Operating at such a fine horizontal resolution, ICON is able to resolve individual clouds (Figure 1). However, ICON only calculates all-sky and clear-sky radiative fluxes. While this data can be used to calculate the total cloud radiative effect, it does not allow for making a distinction between overlapping clouds of different types. Therefore, we calculate the radiative fluxes offline with the line-by-line Atmospheric Radiative Transfer Simulator (ARTS) (Buehler et al., 2018) to isolate the radiative effect of high clouds. This setup allows us to switch the radiative effect of high clouds off in the radiative transfer calculations to better study the radiative effect of high clouds over low clouds.

Since the radiative transfer simulations with ARTS are computationally expensive, we subsample atmospheric profiles on a 1° by 1° grid from one timestep (01.08. 12:00 UTC) of ICON data at native resolution. This subset of 64,800 profiles is used to calculate radiative fluxes with ARTS for three different setups: ARTS-allsky including

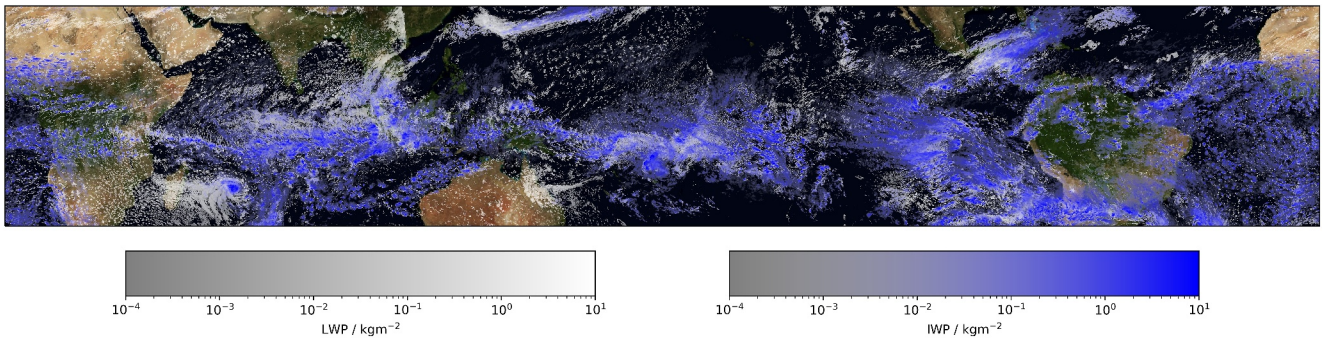

Figure 1. Clouds within ICON at the timestep used within this study. Liquid and frozen clouds are visualized by their liquid water path (LWP) and ice water path (IWP).

all clouds, ARTS-clearsky including no clouds, and ARTS-lowcld including only liquid hydrometeors. We use the ARTS configuration introduced by Brath et al. (2024), which describes the optical properties of frozen hydrometeors as follows: cloud ice is assumed as hexagonal columns and follows the size distribution specified by Geer and Baordo (2014), snow as 10-plate-aggregates with the size distribution from Field et al. (2007) and graupel as droxtals with the size distribution from Doms et al. (2021). Since ARTS is a spectrally resolving radiative transfer model, we prescribe a frequency grid for its simulations. We use 10,000 frequencies which are linearly spaced from 10 cm^{-1} to $5 \cdot 10^3$ cm^{-1} to calculate the radiative transfer in the long-wave regime and another 10,000 frequencies spaced logarithmically from 10^3 cm^{-1} to 10^5 cm^{-1} for the short-wave regime. The distribution of I is calculated from the same ICON timestep, but without subsampling. We limit our analysis to the tropics (30°S to 30°N), which are associated with deep convection whose detrained cloud condensate forms into high clouds.

3. Ice Water Path Framework

The basic idea of the ice water path framework is to treat the radiative properties of high clouds as a function of the cloud thickness, approximated by I, the vertical integral of the sum of all frozen hydrometeors (cloud ice, snow, and graupel). This perspective unravels how the net high-cloud radiative effect changes from positive to negative with increasing I (Figure 2). For the radiative effect of all high clouds, not only $C(I)$ is important, but also the frequency of occurrence of I ($P(I)$). The product of $C(I)$ and $P(I)$ shows the relative importance of high clouds with a specific I for the mean high-cloud radiative effect $\overline{C}$, which is proportional to the area under the $C(I) \cdot P(I)$ curve.

We define high clouds as all clouds with cloud tops above 350 hPa. This includes frozen clouds as well as deep convective clouds which contain frozen and liquid hydrometeors. A similar definition is used by Haslehner et al. (2024), to avoid artificial separation of clouds which can occur if high clouds are defined as frozen clouds. To classify as part of a high cloud, we furthermore require the liquid cloud condensate to sufficiently overlap with the frozen cloud condensate in the vertical (Section 9.2). Any liquid clouds that are not part of a high cloud, we refer to as low clouds. According to this definition, we exclude frozen clouds with cloud tops below 350 hPa from our analysis, which make up for 14% of all frozen clouds.

Based on our definition of high clouds, we calculate C as the difference between the net radiative fluxes at TOA including the radiative effect of high clouds (F_{allsky}) and without the radiative effect of high clouds (F_{nohcld}):

$$C = F_{\text{allsky}} - F_{\text{nohcld}},$$

where F_{nohcld} can originate from regions with low clouds or from clear-sky regions:

$$F_{\text{nohcld}} = \begin{cases} F_{\text{lowcld}}, & \text{if low cloud below,} \\ F_{\text{clearsky}}, & \text{if no cloud below.} \end{cases}$$

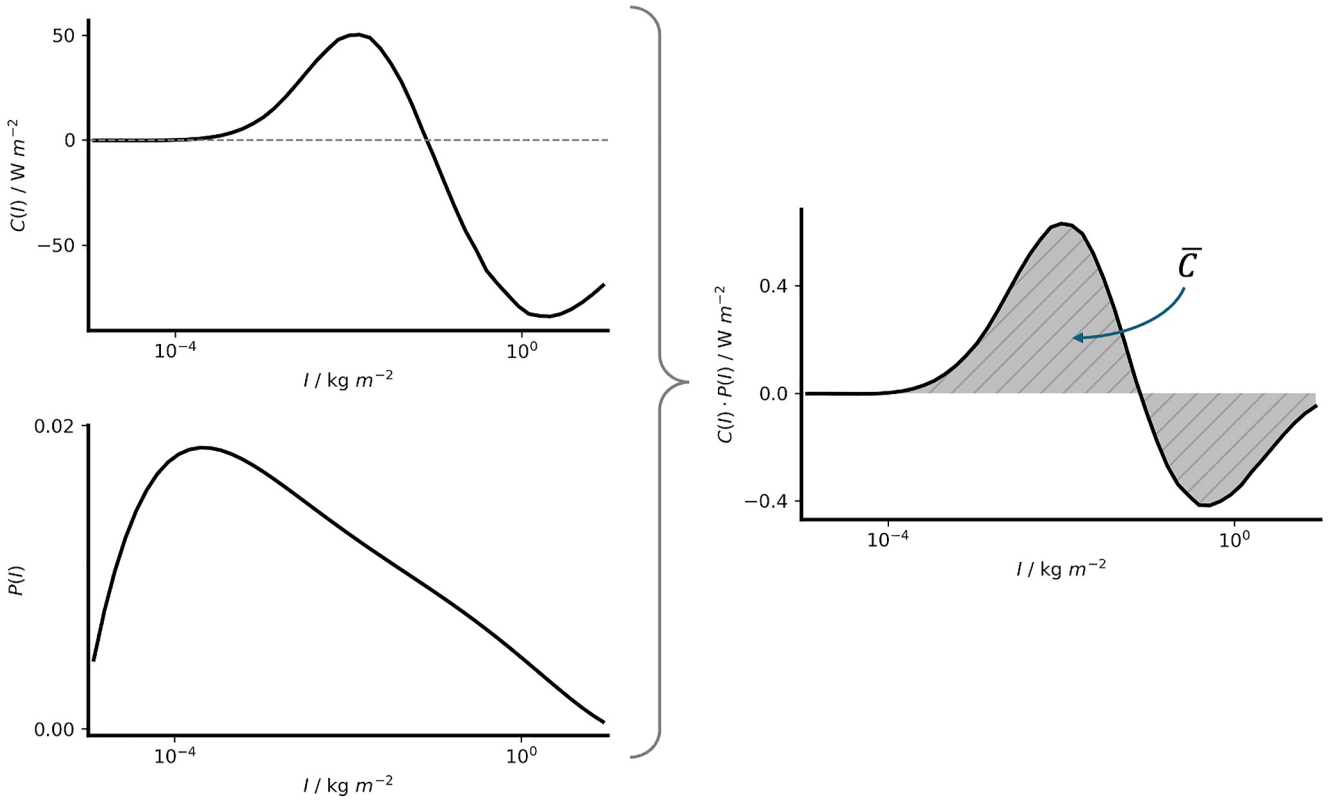

Figure 2. Schematic of how the mean high-cloud radiative effect $(\overline{C})$ is calculated from the net high-cloud radiative effect as a function of ice water path $(C(I))$ and the ice water path distribution $(P(I))$. $\overline{C}$ is proportional to the shaded area under the curve of $C(I) \cdot P(I)$.

All radiative fluxes are co-located since they are calculated for the same grid points but with their respective ARTS setup. We split up the radiative spectrum into a LW and a SW contribution. The net value of C (C_{net}) is calculated as the sum of the SW (C_{SW}) and LW contributions (C_{LW}).

To simplify our analysis, we neglect the influence of the timing of convection on $C(I)$. It has been shown that the occurrence frequency of high clouds does vary over the day due to peaks of deep-convective activity in the morning (over ocean) and in the afternoon (over land) (Gasparini et al., 2022). This will affect $C(I)$, because if a certain I is more likely to occur during day than during night, the corresponding $C_{\text{net}}(I)$ will be more negative due to a stronger SW component. We neglect this dependence by assuming that every I is equally likely to occur at any time of the day. This simplification is necessary to keep the conceptual model of $C(I)$ sufficiently simple to allow for intuitive conclusions. To calculate $C(I)$ in agreement with this simplification, we bin C by I and longitude, interpolate this 2D field linearly and average over all longitudes to calculate $C(I)$. A similar simplification is made by Wall and Hartmann (2018), who show that the resulting bias in the mean $C_{\text{net}}(I)$ is negligible.

Sorting the atmospheric profiles by I allows us to link the thickness of high clouds to their radiative effect (Figure 3). Since I spans several orders of magnitude, we interpret our results in $\log_{10}(I)$ space. This reveals that thick clouds characterized by high I which are typically part of deep convective towers exert a negative C_{net} since the negative SW dominates over the positive LW contribution. This balance shifts for anvil clouds of intermediate thickness at $I = 6 \cdot 10^{-2}$ kg m^{-2}, below which C_{net} is positive. The maximum C_{net} of 45 W m^{-2} occurs at $I = 1.3 \cdot 10^{-2}$ kg m^{-2}. Moving from this I toward lower values associated with thin cirrus clouds, C_{net} converges to zero.

The shape of $C_{\text{net}}(I)$ diagnosed by us is similar to estimates from radiative convective equilibrium (RCE) simulations and satellite observations, however the curves are shifted to higher I with the transition from positive to negative values occurring at: $I = 2 \cdot 10^{-1}$ kg m^{-2} for RCE (Sokol et al., 2024), and $I = 1.2 \cdot 10^{-1}$ kg m^{-2} for satellite observations (Gasparini et al., 2019). We assume that the lower sensitivity of C_{net} to I found by Gasparini

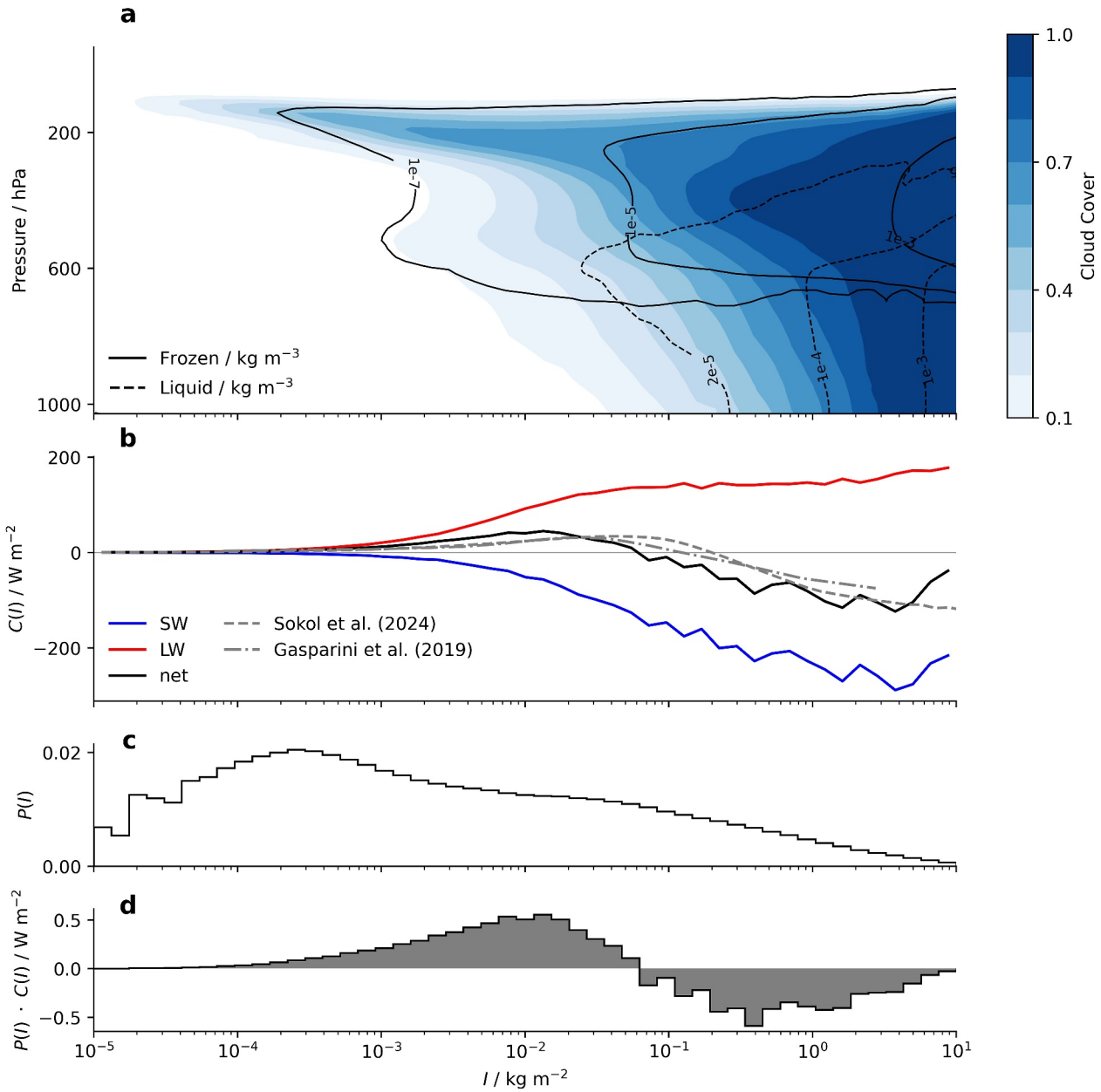

Figure 3. Filled contours of cloud cover and contour lines of frozen and liquid water content (a), Cloud radiative effect C from ARTS and the net C from Sokol et al. (2024) and Gasparini et al. (2019) (b), Ice water path distribution P from ICON (c) and the net C from ARTS weighted by P (d). All quantities are plotted against the ice water path I.

et al. (2019) compared to ARTS is due to differences in horizontal resolution. The observed radiative fluxes used by Gasparini et al. (2019) to derive C have a horizontal resolution of 30 km, which is coarse compared to the 5 km of horizontal grid spacing used by us and can lead to the inclusion of clear-sky contributions in C_{net}, which would lower its sensitivity to I. The RCE models are run at 3 km horizontal grid spacing, hence we suspect that the differences in $C_{\text{net}}(I)$ compared to ARTS result from differences in how frozen hydrometeors are treated within the radiative transfer schemes. This disagreement gives rise to the question of how robust the mapping from frozen condensate mass to radiative fluxes is with respect to different assumptions about the optical properties of the hydrometeors. We are trying to answer that question within a different study by altering the optical properties of the hydrometeors assumed within ARTS (Section 2) to generate a model ensemble which allows us to quantify the resulting uncertainty in $C(I)$.

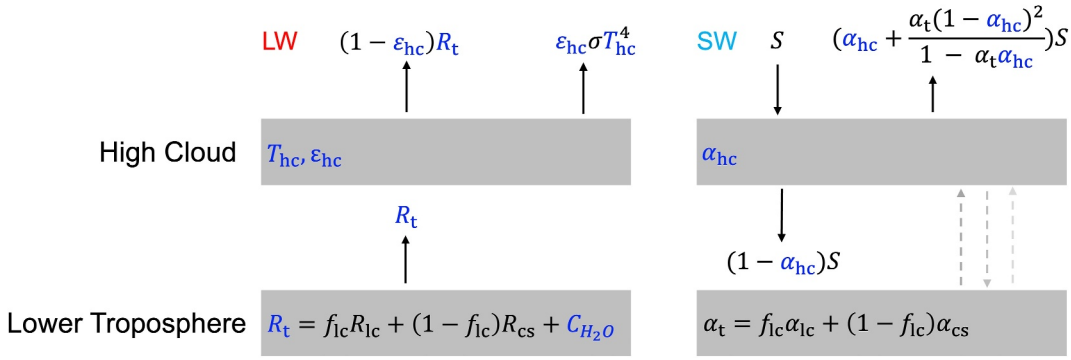

Figure 4. Schematic of the conceptual model, distinguishing between the short wave (SW) and long wave (LW) component of the high-cloud radiative effect. Variables that depend on I are marked in blue. See Table 2 for variable descriptions.

The distribution of I ($P(I)$), calculated as the fraction of profiles within the tropics covered by the respective I, reveals that thin high clouds with a weakly positive C_{net} are more frequent than thick high clouds with a strongly negative C_{net}. At the maximum of P at $I = 3 \cdot 10^{-4}$ kg m^{-2}, we find $C_{net} = 4.2$ Wm^{-2}.

The mean high-cloud radiative effect $(\overline{C})$ is calculated as

$$\overline{C} = \sum_I C(I) \cdot P(I).$$

The usual weighting of gridcells with cos(latitude) is not necessary here since gridcells of ICON are to first order equal in area. Inspecting the product of $C(I)$ and $P(I)$ shows that both are equally important for $\overline{C}$. Thin clouds with a weakly positive $C_{net}(I)$ occur frequently enough to slightly overcompensate the contribution from less frequent thick high clouds with a strongly negative $C_{net}(I)$. Therefore, we find that high clouds in this ICON simulation are on average slightly warming the Earth with $\overline{C_{net}} = 1.25$ W m^{-2}. This is higher than the -1.5 Wm^{-2} estimated by McKim et al. (2024), but reasonably close to the 2 Wm^{-2} from L'Ecuyer et al. (2019), with both estimates relying on satellite observations. We hypothesize that the disagreement between our estimate and the one from McKim et al. (2024) is due to the fact that they do not properly account for the effect of overlapping low clouds in their study (Section 6).

4. Conceptual Model of the High-Cloud Radiative Effect

To understand what sets C and how it might change with warming, we develop a conceptual model that predicts C as a function of I to reduce the complexity of C to a minimum (Figure 4). We approximate high clouds as a single layer characterized by cloud top temperature (T_{hc}), long wave emissivity (ε_{hc}) and short wave albedo (α_{hc}), which are functions of I. Anything below the high clouds is referred to as the lower troposphere (subscript t), which is characterized by an upward LW flux (R_t) and a short wave albedo (α_t). Both R_t and α_t are composed by a contribution from clear-sky regions and low clouds based on the low cloud fraction (f_{lc}). For $R_t(I)$, we furthermore introduce a correction term $C_{H_2O}(I)$ that accounts for the reduction of R_t with increasing I due to the moistening of the atmosphere that outweighs the increase in surface temperature.

For the LW radiation, we assume that R_t penetrates the high cloud depending on ϵ_{hc} and that the high cloud emits LW radiation to space with the same emissivity according to the Stefan-Boltzmann law. The all-sky LW flux at TOA ($F_{LW,allsky}$) is therefore given as

$$F_{LW,allsky}(I) = -(1-\varepsilon_{hc}(I))R_t(I) - \varepsilon_{hc}(I)\sigma T_{hc}(I)^4,$$

with upward fluxes being defined as negative. To calculate $C_{LW}(I)$, we subtract the LW flux at TOA without high clouds ($\varepsilon_{hc} = 0$) from $F_{LW,allsky}$:

$$C_{\mathrm{LW}}(I) = \left[-(1-\varepsilon_{\mathrm{hc}}(I))\,R_{\mathrm{t}}(I) - \varepsilon_{\mathrm{hc}}(I)\sigma T_{\mathrm{hc}}(I)^4\right] - \left[-R_{\mathrm{t}}(I)\right] = \varepsilon_{\mathrm{hc}}(I)\left(R_{\mathrm{t}}(I) - \sigma T_{\mathrm{hc}}(I)^4\right). \quad (1)$$

For the SW radiation, we assume that the incoming solar radiation (S) penetrates the high cloud based on α_{hc}. The remaining SW radiation will experience multiple reflections between the high cloud and the lower troposphere, which are described by a harmonic series that converges (Section 9.3). The all-sky SW flux at TOA ($F_{\mathrm{SW,allsky}}$) is therefore given as

$$F_{\mathrm{SW,allsky}} = S - S\left(\alpha_{\mathrm{hc}}(I) + \frac{\alpha_{\mathrm{t}}(1-\alpha_{\mathrm{hc}}(I))^2}{1-\alpha_{\mathrm{hc}}(I)\alpha_{\mathrm{t}}}\right)$$

To calculate C_{SW}, we subtract the SW flux at TOA without high clouds ($\alpha_{\mathrm{hc}} = 0$) from $F_{\mathrm{SW,allsky}}$:

$$C_{\mathrm{SW}}(I) = \left[S - S\left(\alpha_{\mathrm{hc}}(I) + \frac{\alpha_{\mathrm{t}}(1-\alpha_{\mathrm{hc}}(I))^2}{1-\alpha_{\mathrm{hc}}(I)\alpha_{\mathrm{t}}}\right)\right] - \left[S - \alpha_{\mathrm{t}}S\right] = S\left(\alpha_{\mathrm{t}} - \alpha_{\mathrm{hc}}(I) - \frac{\alpha_{\mathrm{t}}(1-\alpha_{\mathrm{hc}}(I))^2}{1-\alpha_{\mathrm{hc}}(I)\alpha_{\mathrm{t}}}\right). \quad (2)$$

For both SW and LW radiation we do not explicitly include emission and extinction from the atmosphere above high clouds.

5. Key Ingredients of the High-Cloud Radiative Effect

We use the ARTS simulations to determine the free parameters of the conceptual model (Section 9.4). The shape of the mean of T_{hc} binned by I is closely linked to the cloud top height (compare Figures 3a and 5a). The thickest clouds penetrate into the tropopause, resulting in cold cloud top temperatures. Clouds of intermediate thickness are generally lower and warmer, while the thinnest clouds are again found at higher, colder levels. We define $T_{\mathrm{hc}}(I)$ as the mean T_{hc} binned by I, since this relationship does not follow a clear functional form, which would allow for further simplification.

The mean values of $\varepsilon_{\mathrm{hc}}$ and α_{hc} binned by I follow an S-shape in the $\log_{10}(I)$ space, that is, they approach zero for small I and a constant for large I with a transition for intermediate values (Figures 5b and 5d). Therefore, we approximate $\varepsilon_{\mathrm{hc}}(I)$ and $\alpha_{\mathrm{hc}}(I)$ with logistic functions. Values of $\varepsilon_{\mathrm{hc}}$ higher than one can result from a bias of T_{hc}, or the approximation that LW radiation emitted by the high clouds escapes to space without further atmospheric absorption (Figure 4). Since the mean of $\varepsilon_{\mathrm{hc}}$ binned by I does not overshoot values of one significantly, we regard those simplifications to be acceptable (Figure 5b). Besides of I, α_{hc} also depends on the incoming solar radiation (Figure 5d). If the sun is closer to the horizon, the path of the SW radiation through the cloud and hence α_{hc} increase. We eliminate this dependency by calculating the daily mean α_{hc} (Section 9.4.3).

The radiative properties of the lower troposphere are governed by clear-sky regions and low clouds. The mean fraction of low clouds binned by I stays roughly constant for all I (Figure 5c). Therefore, we approximate f_{lc} to be constant at the mean value of f_{lc} averaged over all I with $f_{\mathrm{lc}} = 0.16$. Interestingly, the binned mean f_{lc} stays roughly constant even though the fraction of gridcells with LWP $> 10^{-4}$ kg m^{-2} increases strongly with I beyond $I > 10^{-1}$ kg m^{-2}. This means that high clouds contain increasingly more liquid condensate at high I, causing the fraction of low clouds to remain roughly constant.

Based on f_{lc}, we calculate α_{t} as a composition of a clear-sky and a low-cloud contribution (Figure 4). The rationale behind this approach is that we can distinguish between the high albedo of low clouds and the lower albedo of clear-sky regions (Figure 5f). We use the same approach to describe how R_{t} is composed by a strong flux from clear-sky and a weaker flux from low cloud regions (Figure 5e). However, the magnitude of R_{t} also depends on I. R_{t} decreases with I due to a moistening of the atmosphere that outweighs an increase in surface temperature. This decrease of R_{t} with I is approximated by the correction term $C_{\mathrm{H_2O}}$ that scales linearly with $\log_{10}(I)$ (Section 9.4.4).

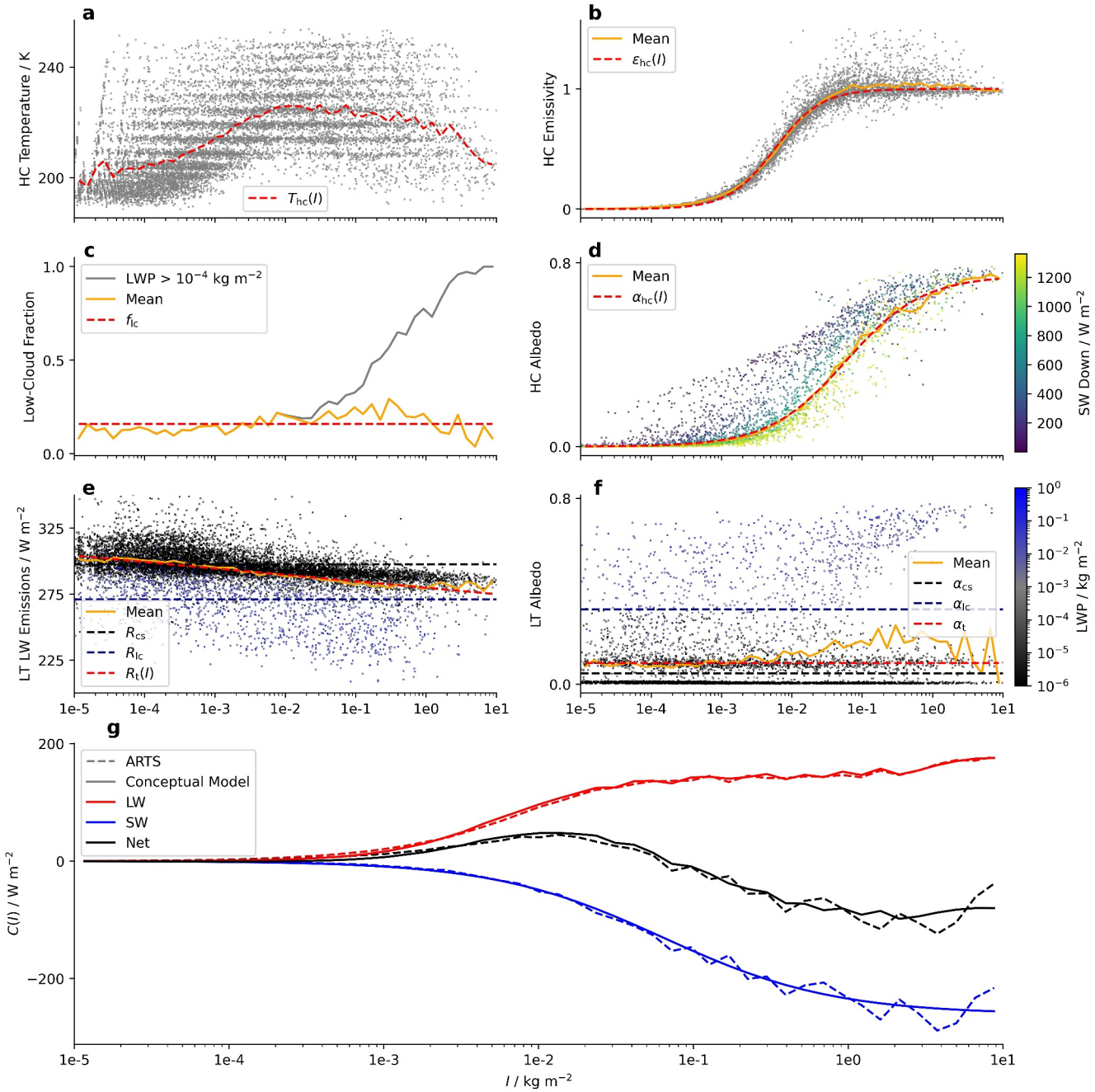

Figure 5. All input variables of the conceptual model (a–f) and the resulting high-cloud radiative effect C as a function of the ice water path I (g). Dots in a–f show individual atmospheric profiles, solid orange lines the mean binned by I and red dashed lines denote model inputs of high cloud (HC) and lower troposphere (LT) variables.

Feeding those radiative properties of high-clouds and the lower troposphere into the conceptual model allows us to predict the high-cloud radiative effect (Equations 1 and 2). The conceptual model seems to capture the main physics underlying $C(I)$, since it is able to reproduce the shape of $C(I)$ from the ARTS simulations (Figure 5g). The agreement between $C(I)$ from ARTS and the conceptual model also shows in $\overline{C}$. The error of the conceptual model compared to ARTS is 0.45% for $\overline{C_{SW}}$, 0.4% for $\overline{C_{LW}}$, and 0.8% for $\overline{C_{net}}$ (Table 1). Since $\overline{C_{net}}$ is the small residual of

Table 1
$\overline{C}$ From the ARTS Simulation and the Conceptual Model

Source	SW/Wm^{-2}	LW/Wm^{-2}	Net/Wm^{-2}
ARTS	−28.64	29.89	1.25
Conceptual Model	−28.51	29.77	1.26

two larger numbers, this low relative error in $\overline{C_{\text{net}}}$, which is the result of partial cancellation of errors in $\overline{C_{\text{SW}}}$ and $\overline{C_{\text{LW}}}$, is encouraging.

The conceptual model reduces the complexity of $C(I)$ significantly, and therefore allows to understand what governs the relationship between C and I. The increasingly negative C_{SW} toward high I is solely a result of the increase of α_{hc} with I. On the other hand, C_{LW} is governed by T_{hc} and ε_{hc}. The initial increase of C_{LW} up to $I = 10^{-1}$ kg m^{-2} can be linked to the increase of ε_{hc}. Beyond this I, high clouds are opaque to LW radiation with $\varepsilon_{\text{hc}} \approx 1$ and the continued increase of C_{LW} is caused by the decrease of T_{hc}.

The reduction of complexity involved in $C(I)$ we achieve by using I as the predictor of C comes at the cost of neglecting other factors that influence C. A major simplification we make is to not consider the effect of ice particle properties, such as their effective radii and number concentration, which might affect $C(I)$ if they change, for example, due to aerosols (Beer et al., 2024). Furthermore, we do not take into account that the effect of ice condensate on radiation per ice water content may be different for different hydrometeors, with larger particles having a weaker extinction per ice water content (e.g., Feng et al., 2024). This is confirmed by our ARTS simulation, for which cloud ice causes around 88% of C, even though it only makes up for 10% of the total atmospheric ice mass within the tropics. Therefore, it can be a good alternative to our approach of using the vertical integral of the sum of all ice hydrometeors (cloud ice, snow, and graupel) as a predictor of C to only rely on cloud ice. However, using the vertical integral of cloud ice as a predictor for C would mean to miss the approximately 12% of C caused by snow and graupel and prevent the comparison of models to satellite observations, which typically provide I and hence include all ice species (discussed in more detail in Section 9.1).

Table 2
All Variables Used by the Conceptual Model With Variable Description and Value if It is Constant

Variable	Description	Constant value
I	Ice water path	
T_{hc}	High-cloud temperature	
α_{hc}	High-cloud albedo	
ε_{hc}	High-cloud emissivity	
R_{t}	LW emissions from lower troposphere	
$C_{\text{H}_2\text{O}}$	Moisture correction term	
f_{lc}	Low-cloud fraction	0.16
α_{t}	Lower troposphere albedo	0.09
S	Incoming SW radiation	395 W m^{-2}
L_{α}	Maximum high-cloud albedo	0.74
L_{ε}	Maximum high-cloud emissivity	1
k_{α}	Steepness high-cloud albedo	1.8
k_{ε}	Steepness high-cloud emissivity	3
x_{α}	Midpoint high-cloud albedo	−1.2
x_{ε}	Midpoint high-cloud emissivity	−2.2
R_{lc}	LW emissions from low clouds	271 W m^{-2}
R_{cs}	LW emissions from clear-sky	297 W m^{-2}
α_{lc}	Low-cloud albedo	0.32
α_{cs}	Clear-sky albedo	0.05
a	Slope of $C_{\text{H}_2\text{O}}$	4.9 W m^{-2}
b	Intercept of $C_{\text{H}_2\text{O}}$	13.5 W m^{-2}

6. Low Clouds Render the High-Cloud Radiative Effect Positive

The high-cloud radiative effect depends not only on the radiative properties of high clouds, but also on the assumption of what would be there instead of the clouds, if they were missing. Therefore, low clouds have the potential to alter C. The impact of low clouds on C becomes visible by comparing $C(I)$ from ARTS for cases with low clouds $\left(\text{LWP} > 10^{-4} \text{ kg m}^{-2}\right)$ and without low clouds $\left(\text{LWP} < 10^{-4} \text{ kg m}^{-2}\right)$ (Figure 6). Low clouds reduce the magnitude of the SW part of $C(I)$ more strongly than the LW part, which results in C becoming more positive for all I. This is a result of how low clouds change the boundary conditions of C. They are much brighter but only slightly colder than the clear-sky surface, and therefore decrease the contrast between high clouds and the lower troposphere more strongly in the SW than in the LW spectrum.

Via this mechanism, the amount of low clouds can change the mean high-cloud radiative effect. We show this by calculating $\overline{C}$ with our conceptual model for various values of f_{lc}. Increasing amounts of low clouds render $\overline{C_{\text{net}}}$ more positive (Figure 7). A doubling of $f_{\text{lc}} = 0.16$ diagnosed from this ICON simulation leads to an increase of $\overline{C_{\text{net}}}$ by 102%. The linear relationship between f_{lc} and C is a result of f_{lc} altering the lower tropospheric radiative properties linearly within the conceptual model (Figure 4).

This effect of cloud overlap is difficult to analyze with conventional satellite and model products, which only provide clear-sky and all-sky fluxes. The cloud radiative effect (CRE) calculated from these fluxes includes high and low clouds and can hence not be interpreted as a measure of C. The negative radiative effect of warm and bright low clouds is included in the CRE and will offset the SW contribution from high clouds to more negative values. This becomes visible in the CRE calculated from satellite observations for the tropical west pacific by Gasparini et al. (2019), which remains negative even for the smallest I. Their result should hence not be

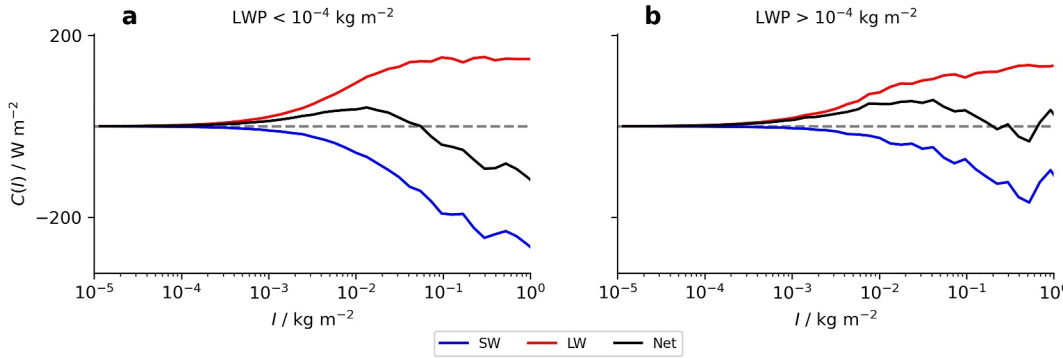

Figure 6. High-cloud radiative effect (C) from ARTS as a function of ice water path (I) without low clouds being present below the high clouds (a) and with low clouds (b).

interpreted, as the CRE of high clouds, but as the CRE of a region that contains a lot of high clouds, together with some low clouds. We hypothesize that the estimate of $\overline{C_{\text{net}}}$ from McKim et al. (2024) is 2.75 W m^{-2} more negative than our estimate because they do not properly account for the effect of overlapping low clouds. Since their detection of clouds relies on reflectivities observed from space, low clouds below optically thick high clouds will be obscured, which leads to an underestimation of the cloud overlap effect. Sokol et al. (2024) developed a different approach to calculate C from all-sky and clear-sky fluxes. They calculate an "ice-only" CRE which only includes profiles with frozen clouds, and an "all-sky" CRE which includes frozen and liquid clouds. For their estimate of C, they use the "ice-only" CRE at $I < 10^{-1}$ kg m^{-1} and the "all-sky" CRE at $I > 10^{0}$ kg m^{-1} with a linear transition in-between. While this approach yields a $C_{\text{net}}(I)$ with a shape similar to our estimate, it does not include the effect of overlapping low clouds on C, which increases $C_{\text{net}}(I)$ as we have shown above. We assume that this explains the difference between their estimate of the maximum $C_{\text{net}}(I)$ of 34 Wm^{-2} and our estimate of 45 Wm^{-2}.

7. Toward a Better Understanding of Tropical High-Cloud Feedbacks

The conceptual model can be used as a tool to diagnose $\overline{C}$ and the related feedback from GSRMs or other km-scale data sources. The main improvement compared to earlier approaches of diagnosing the tropical high-cloud feedback is that our conceptual model is able to predict the individual contributions of clouds over the whole I spectrum and how they contribute to the mean high-cloud radiative effect (Figure 8). This enables us to show that $C(I)$ and $P(I)$ are equally important for $\overline{C}$ and how SW and LW contributions cancel out. The ability of the conceptual model to diagnose the contribution of thin high clouds with $\varepsilon_{\text{hc}} < 1$ to $\overline{C}$ improves on the commonly used radiative kernels, which are known to wrongly interpret such clouds as part of a deeper and optically thicker cloud, since their detection algorithm of cloud top height relies on brightness temperature (Zelinka et al., 2012). The approach of Sokol et al. (2024) to diagnose $C(I)$ went into a similar direction as our conceptual model. However, we go one step further by explaining what shapes the relationship between C and I, which enables us to diagnose differences in $C(I)$ between models or climates.

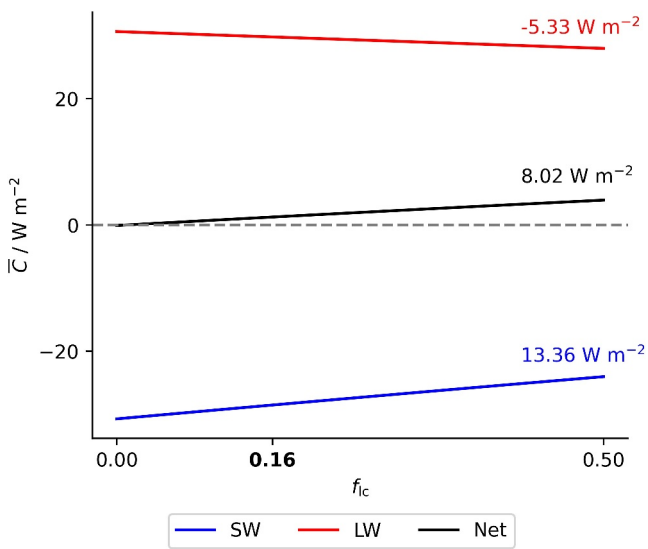

Figure 7. Mean high-cloud radiative effect $\overline{C}$ for different low cloud fractions f_{lc} from the conceptual model. The value of f_{lc} diagnosed from the ICON simulation is indicated in bold. The numbers next to the lines denote the slope of the curves.

By reducing the complexity of $C(I)$, the conceptual model simplifies diagnosing high-cloud feedbacks. If we assume that $\alpha_{\text{hc}}(I)$ and $\varepsilon_{\text{hc}}(I)$ are invariant to surface warming, since the physics of how radiation interacts with cloud condensate do not depend on the climate, the input data we need to diagnose $C(I)$ can be reduced to $T_{\text{hc}}(I)$ and f_{lc}. This means that no additional radiative transfer simulations are necessary. To calculate $T_{\text{hc}}(I)$ and f_{lc} in a way that is consistent with our conceptual model, instantaneous profiles of cloud hydrometeors are needed (Section 9.4).

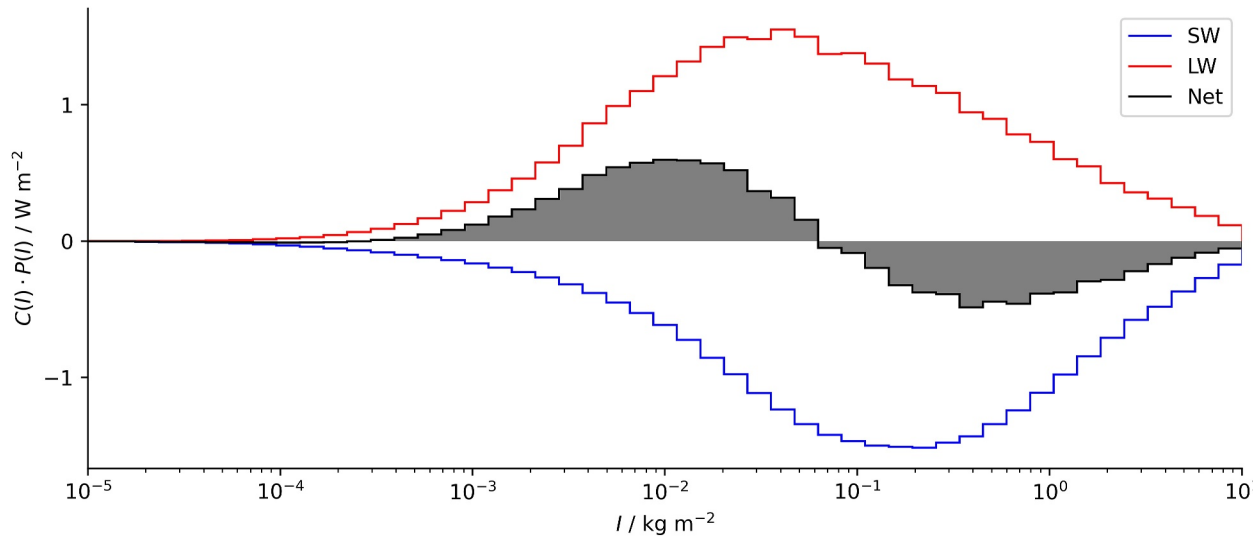

Figure 8. The high-cloud radiative effect ($C(I)$) from the conceptual model, weighted by the ice water path distribution ($P(I)$) from ICON. The area below the curves is proportional to the mean high-cloud radiative effect ($\overline{C}$).

Resolving C as a function of I allows us to investigate how proposed mechanisms of the tropical high-cloud feedback like PHAT (Zelinka & Hartmann, 2010) and the stability iris (Bony et al., 2016) play out across the ice water path spectrum. While PHAT is expected to change $C(I)$, the stability iris effect would affect $P(I)$. Both mechanisms may well apply differently to high clouds of different I, since the processes governing cloud formation and lifetime vary greatly with I, ranging from deep convective clouds to thin cirrus. for example, results from RCE indicate that the stability iris might apply only to thick high clouds with negative $C_{\text{net}}(I)$ (Sokol et al., 2024).

It is possible to apply our conceptual model to GCMs with horizontal grid spacings of $\mathcal{O}$(100 km), but we believe this is less promising than focusing on high-resolution GSRMs. The I that can be derived from GCMs often does not include precipitating hydrometeors and does not compare well with satellite observations (Eliasson et al., 2011). Furthermore, we expect high I associated with deep convection or thick anvils to be less well represented in GCMs compared to GSRMs due to the low horizontal resolution of GCMs. On the other hand, $P(I)$ from GSRMs compares well with satellite observations (Turbeville et al., 2022). As multi-year GSRM simulations become more common (Wieners et al., 2024), we believe that future research on tropical high-cloud feedbacks should focus on GSRM simulations and try to constrain them with satellite observations. Especially satellite products based on active radar and lidar measurements seem promising, as they are able to resolve cloud overlaps (e.g., Matus & L'Ecuyer, 2017).

8. Summary and Conclusion

With this study, we seek to improve the understanding of the high-cloud radiative effect within the tropics by explaining its dependence on the ice water path. This perspective reveals that the radiative effect of a cloud with a specific ice water path and its frequency of occurrence are equally important for its contribution to the mean high-cloud radiative effect. By showing how radiative properties of high clouds depend on the ice water path, we provide a more physical framework for the analysis of high-cloud radiative effect compared to earlier studies assuming high clouds to be uniform (McKim et al., 2024).

For the development of the ice water path perspective on high clouds, we harness the capability of GSRMs to resolve individual clouds in global simulations. We use the atmospheric profiles from ICON with 5 km horizontal grid spacing and calculate radiative fluxes offline with ARTS, which allows us to switch the effect of high clouds off in the radiative transfer calculations. By developing a conceptual model, we demonstrate that the complexity of the high-cloud radiative effect can be reduced significantly if it is interpreted as a function of ice water path. To first order, the dependency of the high-cloud radiative effect on ice water path can be explained by abstracting high clouds as a single layer whose temperature, emissivity and albedo are varying with ice water path. Within

this framework, the lower troposphere below high clouds is characterized by upwelling LW emissions and an albedo. We conceptualize these properties as functions of the low cloud fraction, which determines the contributions from clear-sky and low-cloud regions, with an additional correction term being introduced for the upwelling LW emissions.

The dependence of high-cloud albedo and emissivity on the logarithm of the ice water path is characterized by an S-shape that can be well approximated with logistic functions. While the dependence of the SW high-cloud radiative effect on ice water path is governed only by the high-cloud albedo, the interplay of high-cloud emissivity and temperature explains their LW radiative effect. Up to an ice water path of 10^{-1} kg m^{-2} the LW high-cloud radiative effect increases as a result of increasing high-cloud emissivity. The continued increase of the LW high-cloud radiative effect beyond this ice water path where the high-cloud emissivity reaches one is explained by the decrease of high-cloud temperature. The net high-cloud radiative effect results from a cancellation of SW and LW effects. For thin high clouds below an ice water path of $6 \cdot 10^{-2}$ kg m^{-2} the LW component dominates, hence the net high-cloud radiative effect is positive and converges toward zero for decreasing ice water path. Above an ice water path of $6 \cdot 10^{-2}$ kg m^{-2}, the SW component dominates and the net high-cloud radiative effect becomes negative.

We show that the mean radiative effect of high clouds becomes more positive for increasing amounts of underlying low clouds. This can be understood as a result of low clouds being bright but relatively warm. Therefore, they decrease the contrast of high clouds and the lower troposphere more strongly in the SW than in the LW spectrum, resulting in a stronger decrease in magnitude of the negative SW high-cloud radiative effect compared to its positive LW counterpart. With this cloud overlap effect included, we derive a mean high-cloud radiative effect from the ARTS simulations of 1.25 W m^{-2}, which is closely matched by the conceptual model with 1.26 W m^{-2} While our estimate of the mean high-cloud radiative effect is reasonably close to the 2 Wm^{-2} estimated by L'Ecuyer et al. (2019), it is significantly higher than the -1.5 Wm^{-2} from McKim et al. (2024). We assume that this discrepancy is a result of underestimation of the cloud overlap effect by McKim et al. (2024), since low clouds are obscured by thick high clouds in satellite observations.

Great hopes have been put in the abilities of GSRMs in helping to reduce the uncertainty of cloud feedbacks. The conceptual model based on the ice water path perspective introduced in this study provides a framework for analyzing the tropical high-cloud feedback produced by GSRMs, since it reduces the involved complexity significantly.

9. Methods

9.1. Choosing the Right Predictor for the High-Cloud Radiative Effect

Ice in the atmosphere is typically divided into a number of hydrometeor species within models. The ICON simulation we use distinguishes cloud ice, snow and graupel (Baldauf et al., 2011). Even though cloud ice only makes up for 10% of the total atmospheric ice mass in the tropics, it is the most important hydrometeor for C. If we deactivate snow and graupel in ARTS, C is reduced by only 13% in the SW and 12% in the LW regime. Since the SW and the LW contribution cancel out and the reduction in the SW dominates, C_{net} is increased by 15%.

That cloud ice has a much stronger effect on radiation per unit mass compared to snow and graupel means that I, the vertical integral of all three hydrometeors, might not be a reliable predictor for C. This discrepancy arises because C depends not only on the total amount of ice present in the atmosphere, as measured by I, but also on whether this ice predominantly comprises radiatively active cloud ice or the less radiatively active snow or graupel. However, this issue is mitigated if I serves as a good proxy for the vertical integral of cloud ice (I_{ci}), meaning that the fraction of cloud ice contained in I remains consistent for all I. For the ICON simulation we use, there is a such a clear relationship between I and I_{ci} (Figure 9). The standard deviation of the mean I_{ci} binned by I is around 50% of the mean value for most I, and increases to 100% for high I. Any noise within the relation of I and I_{ci} will result in noise of $C(I)$, as it means the fraction of cloud ice contained in I might vary.

We test how big the increase in noise in $C(I)$ is due to the imperfect relation of I and I_{ci} by comparing the standard deviation of $C(I)$ to the one of the high cloud radiative effect caused by cloud ice (C_{ci}) as a function of I_{ci}. The standard deviation of $C_{\text{ci}}(I_{\text{ci}})$ is indeed generally smaller than that of $C(I)$, but not significantly (Figures 10a and

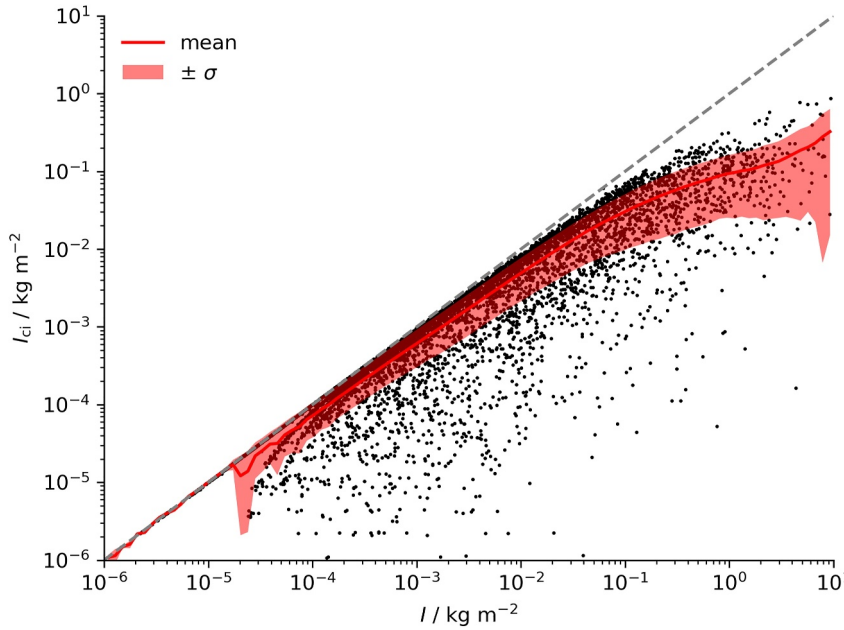

Figure 9. Cloud ice water path I_{ci} plotted against ice water path I for 10,000 randomly chosen profiles (black dots) and the mean I_{ci} binned by I together with ± one standard deviation (red line and red shading).

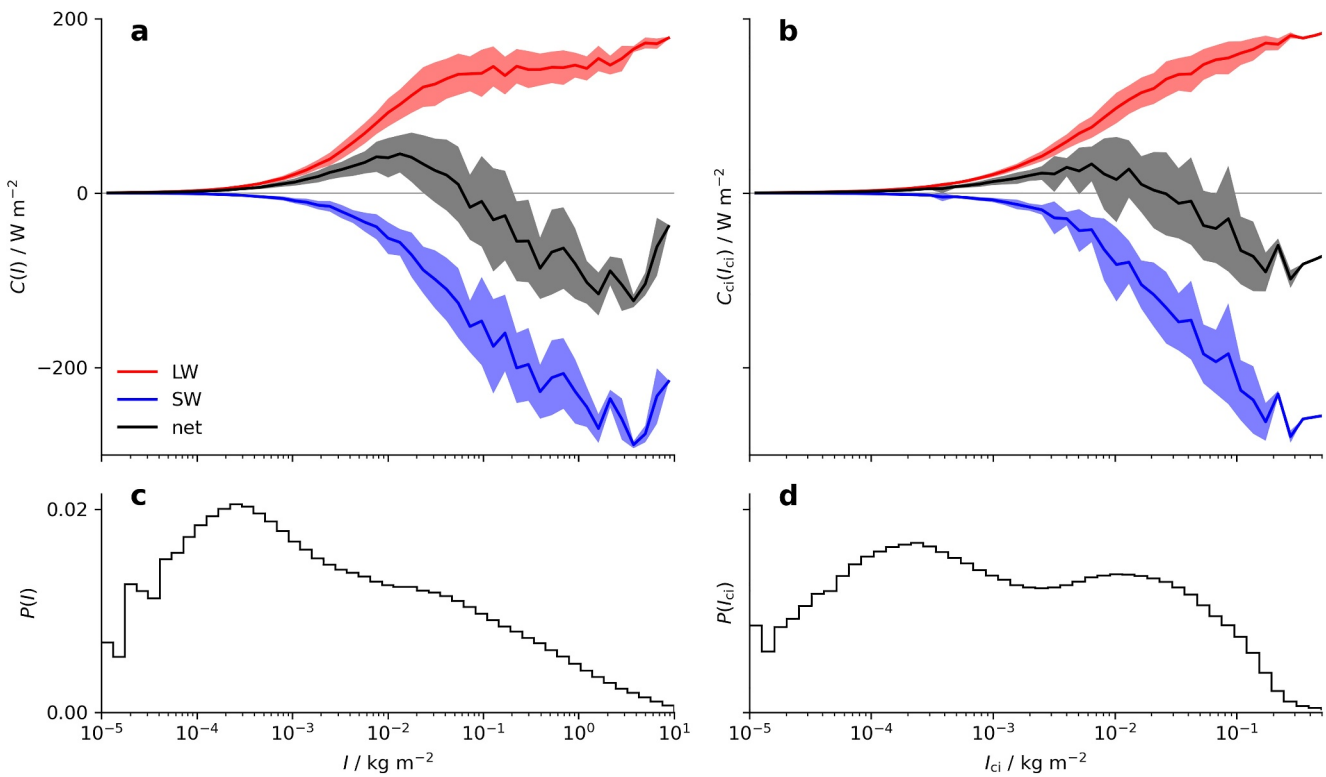

Figure 10. High cloud radiative effect C ± one standard deviation plotted against ice water path I (a) High cloud radiative effect only including cloud ice C_{ci} plotted against cloud ice water path I_{ci} (b). Probability distribution P of ice water path and cloud ice water path (c, d).

10b). The average standard deviation of $C_{ci}(I_{ci})$ in the LW is 6.4 W m^{-2} compared to 10.2 W m^{-2} for $C(I)$ and 12.7 W m^{-2} compared to 16.2 W m^{-2} respectively in the SW.

The general shape of $C_{ci}(I_{ci})$ is comparable to $C(I)$ (Figures 10a and 10b). However, the maximum of I_{ci} is about 1.5 orders of magnitude smaller than the maximum of I, resulting in a more compressed probability distribution (Figures 10c and 10d). It is possible to use I_{ci} within our conceptual model to predict C_{ci}, and doing so does not change our results significantly (not shown). This means that both I and I_{ci} can be used to predict the high-cloud radiative effect.

Whether it is the better choice to include all ice species in the analysis of the high-cloud radiative effect, or not, depends on the question at hand. We believe that for a comparison of several GSRMs, it would be better to exclude less radiatively active ice species and investigate the different $C_{ci}(I_{ci})$, since the partitioning between the ice species may vary strongly between models. However, if a study relies on a single model, or includes satellite observations, we think it is better to use $C(I)$. In this case, we believe that the advantages of this approach of being able to include the radiative effect of all ice species in the high-cloud radiative effect and facilitating the comparison to satellite observations, which typically provide I, outweigh the disadvantage of increasing the noise in the $C(I)$ relationship. Since this study relies only on one model, and we plan to include satellite observations in future studies, we choose to include all ice species in our analysis.

9.2. Connectedness of Clouds

Our definition of high clouds assumes that liquid cloud condensate (q_l) is part of the high cloud if it is connected in the vertical to the frozen condensate (q_f). We assess whether q_l and q_f within one atmospheric column are connected by inspecting the gap between the respective vertical maxima. To this end, we calculate the height at which the maximum concentration of liquid and frozen condensate occurs for every column:

$$z_l = z|_{q_l=\max(q_l)},$$
$$z_f = z|_{q_f=\max(q_f)},$$

where z is the vertical model coordinate. If we can find a grid cell between those levels where the liquid and the frozen condensate are both less than 10% of their respective maximum value within the column, the two phases are considered unconnected:

$$c = \begin{cases} 0, & \exists\ z \in [z_l, z_f] : (q_l < 0.1 \cdot \max(q_l)) \wedge (q_f < 0.1 \cdot \max(q_f)), \\ 1, & \text{Else}, \end{cases} \tag{3}$$

with c being connectedness. Liquid condensate that is not connected to the frozen condensate is interpreted as a low cloud, independent of the high cloud above. Liquid condensate becomes increasingly connected to high clouds for high I (Figure 11). Changing the percentage of the maximum value required for connectedness affects C derived from ARTS. For a threshold of 5% we derive a C_{total} of 1.01 Wm^{-2} and 1.53 Wm^{-2} for 15%. However, this does not affect our qualitative finding that SW and LW contributions to C_{total} cancel out, resulting in a weakly positive net value.

9.3. Conceptualizing Albedo

The SW radiation $(1 - \alpha_{hc})S$ that penetrates the high cloud is partly reflected by the lower troposphere with an albedo α_t, hence $\alpha_t(1 - \alpha_{hc})S$ is reflected by the lower troposphere toward the high cloud. Depending on the high-cloud albedo α_{hc}, a fraction of this upward reflected radiation will penetrate the high cloud, while the rest is reflected back to the lower troposphere and is subject to the same sequence of reflections again. The amount of SW radiation that is reflected by high clouds and the lower troposphere to space (F_{up}) is described by the following series

$$F_{up} = \alpha_{hc}S + \alpha_t(1-\alpha_{hc})^2S + \alpha_{hc}\alpha_t^2(1-\alpha_{hc})^2S + \alpha_{hc}^2\alpha_t^3(1-\alpha_{hc})^2S + \ldots$$

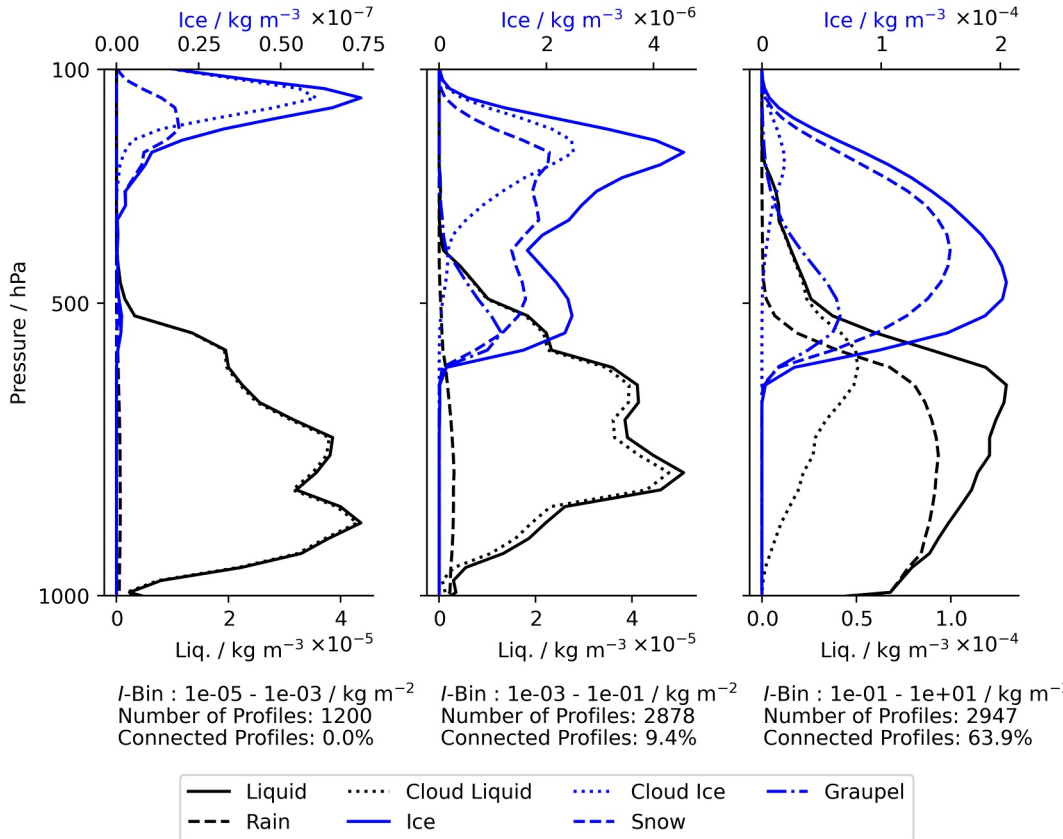

Figure 11. Mean hydrometeor profiles averaged over the respective ice water path I bin for profiles that contain frozen and liquid clouds. The I-bin, the number of profiles within it, and the percentage of those profiles that contain connected liquid and frozen clouds are indicated below each subplot.

This can be rewritten as

$$F_{\text{up}} = S\left[\alpha_{\text{hc}} + \alpha_{\text{t}}(1-\alpha_{\text{hc}})^2\left(1 + \alpha_{\text{hc}}\alpha_{\text{t}} + \alpha_{\text{hc}}^2\alpha_{\text{t}}^2 + \dots\right)\right]. \tag{4}$$

For $\alpha_{\text{hc}} < 1$ and $\alpha_{\text{t}} < 1$ the geometric series from this equation converges

$$\sum_{n=0}^{\infty}(\alpha_{\text{hc}}\alpha_{\text{t}})^n = \frac{1}{1-\alpha_{\text{hc}}\alpha_{\text{t}}}.$$

Therefore, we can rewrite Equation 4 as

$$F_{\text{up}} = S\left(\alpha_{\text{hc}} + \frac{\alpha_{\text{t}}(1-\alpha_{\text{hc}})^2}{1-\alpha_{\text{hc}}\alpha_{\text{t}}}\right).$$

9.4. Parameterizing the Conceptual Model

The parameters of our conceptual model and their dependence on the IWP are inferred from the ARTS simulations. By default, we use all atmospheric profiles from ARTS within the tropics (30°S to 30°N) for the parameterization, except for the 14% of the sample that contain ice clouds with cloud tops below 350 hPa. Only for high-cloud albedo and emissivity, we restrict the parameterization to atmospheric profiles that do not contain low clouds, since this reduces the noise significantly.

9.4.1. Cloud Top Temperature

To diagnose T_{hc} from the ARTS simulations, we identify the cloud top pressure (p_{top}). For thin clouds, we want T_{hc} to correspond to the level from which most LW are emerging. Hence, we calculate the cloud top pressure of thin clouds p_{thin} as the level with the maximum ice water content (IWC, sum of all frozen hydrometeors)

$$p_{thin} = p|_{IWC=\max(IWC)}.$$

However, for thick clouds with $\varepsilon_{hc} = 1$, the LW emissions might emerge from a higher level if enough IWC is located above p_{thin}. To find this emission level of thick clouds, we rely on the considerations of Jeevanjee (2023) and define the vertically integrated ice mass (I, integral downwards from the top) above the emission level as

$$I_{em} = I|_{T_a=T_b},$$

where T_b is the brightness temperature calculated from the spectrally integrated outgoing LW flux at TOA and T_a is the atmospheric temperature. Averaged over all high clouds with IWP $>10^{-1}$ kg m^{-2} for which we assume $\varepsilon_{hc} = 1$, this yields $I_{em} = 6.7 \cdot 10^{-3}$ kg m^2. We use this value to calculate the cloud top pressure of thick clouds (p_{thick}) as

$$p_{thick} = p|_{I=I_{em}}.$$

For a consistent definition of p_{top} over all IWP, we define it as

$$p_{top} = \min(p_{thick}, p_{thin}).$$

T_{hc} is then defined as

$$T_{hc} = T_a|_{p=p_{top}},$$

where T_a is the atmospheric temperature. For the conceptual model, we use the mean value of T_{hc} binned by I.

9.4.2. Emissivity

To calculate ε_{hc}, we require the LW flux at TOA from our conceptual model to match the one from ARTS

$$(1 - \varepsilon_{hc}) R_t + \varepsilon_{hc} \sigma T^4 = F_{LW,allsky}.$$

Since we only include atmospheric profiles without low clouds in this parameterization, R_t simplifies to the clear-sky flux at TOA $(F_{LW,\ clearsky})$. Substituting R_t with $F_{LW,clearsky}$ and rearranging for ε_{hc} yields

$$\varepsilon_{hc} = \frac{F_{LW,allsky} - F_{LW,clearsky}}{\sigma T^4 - F_{LW,clearsky}}$$

The mean ε_{hc} binned by I exhibits a logistic shape in the $\log_{10}(I)$ space (Figure 5b). Since we expect this relationship to be invariant to surface warming, we decrease the complexity of the conceptual model by approximating $\varepsilon_{hc}(I)$ as a logistic function of $\log_{10}(I)$

$$\varepsilon_{hc}(I) = \frac{L_\varepsilon}{1 + \exp\left(-k_\varepsilon\left(\log_{10}(I) - x_\varepsilon\right)\right)}.$$

The parameters within this equation are inferred by fitting it to the binned mean ε_{hc} inferred from the ARTS simulations using non-linear least squares while requiring $L_\varepsilon = 1$, which limits ε_{hc} to a maximum value of 1.

9.4.3. Albedo

To calculate α_{hc}, we require the SW flux at TOA from our conceptual model to match the one from ARTS

$$S - S\left(\alpha_{hc} + \frac{\alpha_t(1-\alpha_{hc})^2}{1-\alpha_{hc}\alpha_t}\right) = S - F_{SW,allsky}, \tag{5}$$

where $F_{SW,allsky}$ is the upward SW flux at TOA. Since we only include atmospheric profiles without low clouds, α_t simplifies to the clear-sky albedo (α_{cs}, compare Figure 4). Dividing Equation 5 by S yields

$$\alpha_{hc} + \frac{\alpha_{cs}(1-\alpha_{hc})^2}{1-\alpha_{hc}\alpha_{cs}} = \frac{F_{SW,allsky}}{S}.$$

The right hand side term represents the all-sky albedo $\frac{F_{SW,allsky}}{S} = \alpha_{as}$. With this, we can rearrange for α_{hc}

$$\alpha_{hc} = \frac{\alpha_{as} - \alpha_{cs}}{1 + \alpha_{cs}(\alpha_{as} - 2)}.$$

To calculate the mean of α_{hc} binned by I we have to consider that α_{hc} depends on the amount of incoming SW radiation (Figure 5d) and that α_{hc} at noon is more important for the daily mean than α_{hc} in the evening when incoming SW radiation is low. Therefore, we bin α_{hc} by I and longitude and interpolate this 2D field linearly to fill potential data gaps. Next, we calculate the mean over all longitudes for each I bin, weighted with the incoming SW radiation. Like ε_{hc}, the mean of α_{hc} binned by I exhibits a logistic shape (Figure 5d). Since we assume that this relationship will also be invariant to surface warming, we decrease the complexity of the conceptual model by approximating $\alpha_{hc}(I)$ as a logistic function of $\log_{10}(I)$

$$\alpha_{hc}(I) = \frac{L_\alpha}{1 + \exp\left(-k_\alpha\left(\log_{10}(I) - x_\alpha\right)\right)},$$

The parameters within this equation are determined by fitting it to the binned mean α_{hc} inferred from the ARTS simulations using non-linear least squares.

9.4.4. Lower Troposphere

The radiative properties of the lower troposphere are parameterized based on the mean fraction of low clouds f_{lc}. To calculate f_{lc}, we compare the LWP to a threshold and require the low cloud not to be connected to a high cloud

$$f_{lc} = \begin{cases} 1, & \forall\ \text{LWP} > 10^{-4}\ \text{kg m}^{-2} \wedge c = 0, \\ 0, & \text{otherwise.} \end{cases}$$

Here, c denotes connectedness as defined in Equation 3. Since the mean of f_{lc} binned by I does not vary significantly with I, we approximate f_{lc} to be constant for all I (Figure 5c).

We calculate α_{cs} and α_{lc} by dividing the upward TOA fluxes $F_{SW,\ clearky}$ and $F_{SW,\ lowcld}$ by S respectively. For α_t, we select from α_{cs} and α_{lc} based on f_{lc}

$$\alpha_t = \begin{cases} \alpha_{cs}, & \forall\ f_{lc} = 0, \\ \alpha_{lc}, & \forall\ f_{lc} = 1. \end{cases}$$

The mean value of α_{cs} is calculated by averaging α_{cs} over all atmospheric profiles with $f_{lc} = 0$. To calculate the average of α_{lc}, we have to take into consideration that, like α_{hc}, it depends on the incoming SW radiation. To calculate the daily mean value of α_{lc}, we therefore apply the same technique as for α_{hc} and bin α_{lc} by LWP and

longitude. We linearly interpolate this 2D field and average over all longitudes. From the resulting α_{lc} binned by LWP, we calculate the mean value as

$$\alpha_{lc} = \frac{\sum_{LWP} \alpha_{lc}(LWP) \cdot n(LWP)}{\sum_{LWP} n(LWP)},$$

where n(LWP) is the number of profiles with $f_{lc} = 1$ per LWP bin.

To derive R_t, we use the TOA fluxes $F_{LW,clearsky}$ and $F_{LW,lowcld}$

$$R_t = \begin{cases} F_{LW,clearsky}, & \forall\ f_{lc} = 0, \\ F_{LW,lowcld}, & \forall\ f_{lc} = 1. \end{cases}$$

For the mean value of R_{cs}, we average $F_{LW,clearsky}$ over all atmospheric profiles with $f_{lc} = 0$. For the mean value of R_{lc}, we average $F_{LW,lowcld}$ over all atmospheric profiles with $f_{lc} = 1$. The approximately linear decrease of the binned mean of R_t with $\log_{10}(I)$ (Figure 5e) can be linked to an increase of integrated column water vapor with I (not shown). To correct for this, we introduce the correction term $C_{H_2O}(I)$, which scales linearly with $\log_{10}(I)$

$$C_{H_2O}(I) = a \cdot \log_{10}(I) + b.$$

The coefficients a and b are inferred from linearly regressing the anomaly of the binned mean of R_t with $\log_{10}(I)$.

Data Availability Statement

The code to reproduce the results and figures presented in this study is available from https://github.com/JakobDeutloff/cm_publication and archived under https://doi.org/10.5281/zenodo.14059493 (Deutloff, 2024). The model data and the parameter sets are archived under https://doi.org/10.25592/uhhfdm.14753 (Deutloff & Brath, 2024). The full ICON simulation which provides the basis for our analysis is made available by Kluft (2023).

Acknowledgments
This research was funded by the Deutsche Forschungsgemeinschaft (DFG, German Research Foundation) under Germany's Excellence Strategy—EXC 2037 "CLICCS—Climate, Climatic Change, and Society"—Project Number: 390683824, contribution to the Center for Earth System Research and Sustainability (CEN) of Universität Hamburg. We thank Brett McKim, Adam Sokol and Blaž Gasparini for inspiring discussions and Lukas Kluft for assisting with the model data. We also want to thank the three anonymous reviewers who helped to improve this manuscript. Open Access funding enabled and organized by Projekt DEAL.

References

Arias, P., Bellouin, N., Coppola, E., Jones, R., Krinner, G., Marotzke, J., et al. (2021). Technical summary [Book Section]. In V. Masson-Delmotte, et al. (Eds.), *Climate change 2021: The physical science basis. Contribution of working group I to the sixth assessment report of the intergovernmental panel on climate change* (pp. 33–144). https://doi.org/10.1017/9781009157896.002

Baldauf, M., Seifert, A., Förstner, J., Majewski, D., Raschendorfer, M., & Reinhardt, T. (2011). Operational convective-scale numerical weather prediction with the COSMO model: Description and sensitivities. *Monthly Weather Review*, *139*(12), 3887–3905. https://doi.org/10.1175/MWR-D-10-05013.1

Beer, C. G., Hendricks, J., & Righi, M. (2024). Impacts of ice-nucleating particles on cirrus clouds and radiation derived from global model simulations with MADE3 in EMAC. *Atmospheric Chemistry and Physics*, *24*(5), 3217–3240. https://doi.org/10.5194/acp-24-3217-2024

Berry, E., & Mace, G. G. (2014). Cloud properties and radiative effects of the Asian summer monsoon derived from A-Train data. *Journal of Geophysical Research: Atmospheres*, *119*(15), 9492–9508. https://doi.org/10.1002/2014JD021458

Bony, S., Stevens, B., Coppin, D., Becker, T., Reed, K. A., Voigt, A., & Medeiros, B. (2016). Thermodynamic control of anvil cloud amount. *Proceedings of the National Academy of Sciences*, *113*(32), 8927–8932. https://doi.org/10.1073/pnas.1601472113

Brath, M., Petersen, J., Buehler, S. A., & Eriksson, P. (2024). Extending the atmospheric radiative transfer simulator (Arts) to shortwave radiation. *Social Science Research Network*. [SSRN Scholarly Paper]. https://doi.org/10.2139/ssrn.4968132

Buehler, S. A., Mendrok, J., Eriksson, P., Perrin, A., Larsson, R., & Lemke, O. (2018). ARTS, the atmospheric radiative transfer simulator – Version 2.2, the planetary toolbox edition. *Geoscientific Model Development*, *11*(4), 1537–1556. https://doi.org/10.5194/gmd-11-1537-2018

Deutloff, J. (2024). Conceptual model code and evaluation scripts (version 1.2.0). *Zenodo*. https://doi.org/10.5281/zenodo.14059493

Deutloff, J., & Brath, M. (2024). High-cloud radiative effect dataset. https://doi.org/10.25592/uhhfdm.14753

Doms, G., Förstner, J., Heise, E., Reinhardt, T., Ritter, B., & Schrodin, R. (2021). *A description of the Nonhydrostatic regional COSMO-model*. Deutscher Wetterdienst.

Eliasson, S., Buehler, S. A., Milz, M., Eriksson, P., & John, V. O. (2011). Assessing observed and modelled spatial distributions of ice water path using satellite data. *Atmospheric Chemistry and Physics*, *11*(1), 375–391. https://doi.org/10.5194/acp-11-375-2011

Feng, J., Menzel, R., & Paynter, D. (2024). A flexible approach to parameterize the optical properties of clouds and precipitation. Retrieved, from https://www.authorea.com/users/563299/articles/1061687-a-flexible-approach-to-parameterize-the-optical-properties-of-clouds-and-precipitation?commit=40b4b1da798bfe338ba57f66b8e6d70b685445ab

Field, P. R., Heymsfield, A. J., & Bansemer, A. (2007). Snow size distribution parameterization for midlatitude and tropical ice clouds. *Journal of the Atmospheric Sciences*, *64*(12), 4346–4365. https://doi.org/10.1175/2007JAS2344.1

Gasparini, B., Blossey, P. N., Hartmann, D. L., Lin, G., & Fan, J. (2019). What drives the life cycle of tropical anvil clouds? *Journal of Advances in Modeling Earth Systems*, *11*(8), 2586–2605. https://doi.org/10.1029/2019MS001736

Gasparini, B., Sokol, A. B., Wall, C. J., Hartmann, D. L., & Blossey, P. N. (2022). Diurnal differences in tropical maritime anvil cloud evolution. *Journal of Climate*, *35*(5), 1655–1677. https://doi.org/10.1175/JCLI-D-21-0211.1

Geer, A. J., & Baordo, F. (2014). Improved scattering radiative transfer for frozen hydrometeors at microwave frequencies. *Atmospheric Measurement Techniques*, *7*(6), 1839–1860. https://doi.org/10.5194/amt-7-1839-2014

Hartmann, D. L. (2016). Tropical anvil clouds and climate sensitivity. *Proceedings of the National Academy of Sciences*, *113*(32), 8897–8899. https://doi.org/10.1073/pnas.1610455113

Haslehner, K., Gasparini, B., & Voigt, A. (2024). Radiative heating of high-level clouds and its impacts on climate. *Journal of Geophysical Research: Atmospheres*, *129*(12), e2024JD040850. https://doi.org/10.1029/2024JD040850

Hohenegger, C., Korn, P., Linardakis, L., Redler, R., Schnur, R., Adamidis, P., et al. (2023). ICON-Sapphire: Simulating the components of the earth system and their interactions at kilometer and subkilometer scales. *Geoscientific Model Development*, *16*(2), 779–811. https://doi.org/10.5194/gmd-16-779-2023

Jeevanjee, N. (2023). Climate sensitivity from radiative-convective equilibrium: A chalkboard approacha. *American Journal of Physics*, *91*(9), 731–745. https://doi.org/10.1119/5.0135727

Kluft, L. (2023). Icon monsoon 2.0 ensemble. *DOKU at DKRZ*. Retrieved from https://hdl.handle.net/21.14106/f8b74dd060c567cb10b56c321add53a3d4618097

L'Ecuyer, T. S., Hang, Y., Matus, A. V., & Wang, Z. (2019). Reassessing the effect of cloud type on Earth's energy balance in the age of active spaceborne observations. Part I: Top of atmosphere and surface. *Journal of Climate*, *32*(19), 6197–6217. https://doi.org/10.1175/JCLI-D-18-0753.1

Matus, A. V., & L'Ecuyer, T. S. (2017). The role of cloud phase in Earth's radiation budget. *Journal of Geophysical Research: Atmospheres*, *122*(5), 2559–2578. https://doi.org/10.1002/2016JD025951

Mauritsen, T., & Stevens, B. (2015). Missing iris effect as a possible cause of muted hydrological change and high climate sensitivity in models. *Nature Geoscience*, *8*(5), 346–351. https://doi.org/10.1038/ngeo2414

McKim, B., Bony, S., & Dufresne, J.-L. (2024). Weak anvil cloud area feedback suggested by physical and observational constraints. *Nature Geoscience*, *17*(5), 1–6. https://doi.org/10.1038/s41561-024-01414-4

Sherwood, S. C., Webb, M. J., Annan, J. D., Armour, K. C., Forster, P. M., Hargreaves, J. C., et al. (2020). An assessment of Earth's climate sensitivity using multiple lines of evidence. *Reviews of Geophysics*, *58*(4), e2019RG000678. https://doi.org/10.1029/2019RG000678

Sokol, A. B., Wall, C. J., & Hartmann, D. L. (2024). Greater climate sensitivity implied by anvil cloud thinning. *Nature Geoscience*, *17*(5), 1–6. https://doi.org/10.1038/s41561-024-01420-6

Turbeville, S. M., Nugent, J. M., Ackerman, T. P., Bretherton, C. S., & Blossey, P. N. (2022). Tropical cirrus in global storm-resolving models: 2. Cirrus life cycle and top-of-atmosphere radiative fluxes. *Earth and Space Science*, *9*(2), e2021EA001978. https://doi.org/10.1029/2021EA001978

Wall, C. J., & Hartmann, D. L. (2018). Balanced cloud radiative effects across a range of dynamical conditions over the tropical west pacific. *Geophysical Research Letters*, *45*(20), 11490–11498. https://doi.org/10.1029/2018GL080046

Wieners, K.-H., Rackow, T., Aguridan, R., Becker, T., Beyer, S., Cheedela, S. K., et al. (2024). nextGEMS: Catalogs of full output of the production simulations for ICON and IFS (Tech. Rep.). *World Data Center for Climate (WDCC) at DKRZ*. Retrieved from https://www.wdc-climate.de/ui/entry?acronym=nextGEMS_prod_addinfov1

Zelinka, M. D., & Hartmann, D. L. (2010). Why is longwave cloud feedback positive? *Journal of Geophysical Research*, *115*(D16). https://doi.org/10.1029/2010JD013817

Zelinka, M. D., Klein, S. A., & Hartmann, D. L. (2012). Computing and partitioning cloud feedbacks using cloud property histograms. Part I: Cloud radiative kernels. *Journal of Climate*, *25*(11), 3715–3735. https://doi.org/10.1175/JCLI-D-11-00248.1

Zelinka, M. D., Klein, S. A., Qin, Y., & Myers, T. A. (2022). Evaluating climate models' cloud feedbacks against expert judgment. *Journal of Geophysical Research: Atmospheres*, *127*(2), e2021JD035198. https://doi.org/10.1029/2021JD035198